LRP 771/03 December 2003

Papers presented at the IAEA Technical Meeting

San Diego, U.SA.
September 2003

Available in colour on the web at
http://crppwww/conferences/

ISSN 0458-5895

LIST OF CONTENTS

Synchronisation of L-mode to H-mode transitions on the sawtooth cycle in ohmic TCV plasmas

Y R Martin and TCV team

Centre de Recherches en Physique des Plasmas, Association Euratom-Confédération Suisse, Ecole Polytechnique Fédérale de Lausanne, CH-1015 Lausanne, Switzerland

Abstract

L-mode to H-mode transitions (LH transitions) are obtained in wide ranges of plasma parameters in TCV ohmic discharges. LH transitions either occur directly, indicated by a single abrupt drop in D_α emission, or present an intermediate 'dithering' phase before the H-mode state is attained, in which the D_α emission shows rapid excursions between L-mode and H-mode levels. The type of transition, with or without a dithering phase, depends on the plasma current and plasma triangularity. It is less sensitive to plasma density and divertor geometry. The relative direction of the ion ∇B drift also plays a role in the characteristics of the LH transition.

The time delay between an LH transition and the preceding sawtooth crash has been measured in every TCV H-mode discharge. Most LH transitions are found to occur in the first 30% of the sawtooth cycle, i.e. in the first 2ms after a sawtooth crash. Moreover, LH transitions often occur soon after the large crash of a 'double sawtooth'. The distribution function of these time delays clearly indicates a synchronisation of these two processes. However, the heat pulse released during a sawtooth crash has a transit time from the q=1 surface to the plasma edge that is much shorter than the time delay between the sawtooth crash and the LH transition.

1. Introduction

LH transitions are generally obtained in diverted plasmas when the additional heating power exceeds a threshold. A power law scaling has been developed to give the minimum power required to obtain a transition in a plasma of a given density and size, in a given magnetic field [1]. This scaling constitutes, up-to-now, the best method to predict the accessibility to the H-mode. However, the uncertainty of the fit is large and its origin is not

yet understood. In order to increase the accuracy of predictions a better understanding of the LH transition physics is necessary.

TCV, with its high shaping capability, is a perfect tool to investigate the effect of other parameters on the accessibility of the H-mode. A large number of LH transitions have been obtained in a wide variety of plasma parameters. Most are obtained in ohmic plasmas when the plasma divertor is formed. A database containing all these LH transitions was compiled and is briefly presented in section 2.

In this paper, two questions are addressed. The first one deals with the type of transition. It is widely recognised that transitions are either direct or in 2 stages with a dithering phase in between. The distribution of the different transition types in the operational domain is discussed in section 3. The second question deals with the influence of the sawtooth cycle on the LH transition physics. Different experiments have already shown that transitions are sometimes synchronised with a sawtooth [2]. Section 4 presents two approaches which lead to the result that most LH transitions are synchronised with sawteeth in TCV. Conclusions are given in section 5.

2. Data Set

All the LH transitions observed in TCV were manually identified on the basis of the D_α emission and the time of their occurrence stored. A database containing these times and the

Parameter	Limiter	Single Null IGRADB=-1	Single Null IGRADB=1	Double Null IGRADB=-1	Double Null IGRADB=1
Nb	32	382	340	39	146
I_p [MA]	0.3 - 0.65	0.3 - 0.5	0.23 - 0.45	0.25 - 0.45	0.23 - 0.5
n_e [$10^{19}m^{-3}$]	5 - 11	3 - 8.5	2.5 - 10	4.5 - 13	4 - 11
κ	1.3 - 2.2	1.4 - 2.0	1.2 - 2.0	1.4 - 1.7	1.3 - 1.7
δ	0.2 - 0.55	0.45 - 0.65	0.25 - 0.65	0.55 - 0.75	0.55 - 0.8
Δ_{in} [mm]	0	5 - 40	1 - 50	5 - 25	1 - 30
R(Xpt) [mm]	0 - 50	10 - 70	0 - 100	0 - 50	0 - 55

Table 1: Operational domain where LH transitions were obtained, for different plasma configurations. Nb, I_p, n_e, κ, δ, Δ_{in} and R(Xpt) are the number of occurrences, plasma current, density, elongation, triangularity, plasma to inner wall distance and radial distance of the major X-point from the inner wall, respectively.

values of many plasma parameters taken at these times was compiled. Data from about 900 plasma discharges are contained in the database. Table 1 shows how the transitions range in the operational domain for different pairs of plasma configurations and the ion ∇B drift direction relative to the position of the major X-point. IGRADB=1 is the favourable case, i.e. the ion ∇B drift is directed towards the X-point.

In order to extract reliable statistics from the database only the 3 most populated classes (column 3, 4 and 6) are studied and are labelled SND-, SND+ and DND+, respectively.

3. LH transition types

One of the signatures of an LH transition is a sudden drop in the D_α emission. However, in some cases a dithering phase may precede the establishment of the H-mode. Figure 1 shows the two different transition types. In the top case, one direct transition occurs, hereafter called 'dLH', and, in the bottom case, one indirect transition occurs, in which a first transition from L-mode to Dithering, 'LD', is followed by a Dithering to H-mode transition 'DH'.

In Single Null discharges with the unfavourable ion ∇B drift (SND-), the transitions are predominantly direct ones (dLH) as shown in Table 2. In the same configuration but with the favourable ion ∇B drift as many direct as indirect transitions were observed. Finally, in Double Null discharges, most of the transitions exhibit a dithering phase. The type of transition then strongly depends on the plasma configuration. It is worth noting the large number of direct transitions in the first

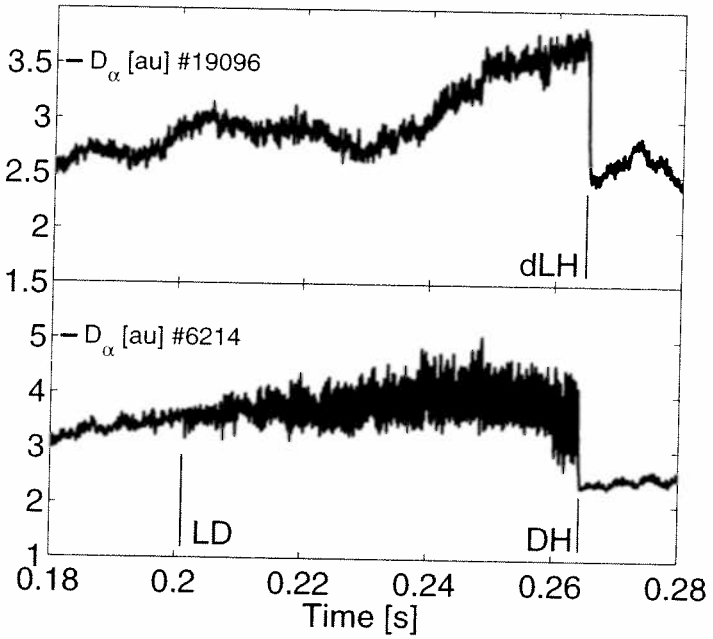

Figure 1: Evolution of the D_α emission for two LH transition types. Top: a direct LH transition, indicated by the vertical line and dLH labelling. Bottom: an LH transition with a dithering phase. The beginning and the end of the dithering phase are considered as LD and DH transitions, respectively.

	dLH (direct)	LD-DH (with dithering)
SND -	367	15
SND +	170	170
DND +	41	105

Table 2: Number of transitions in both classes for the different TCV configurations

case (SND-). Since LH transitions are obtained in approximately the same operational ranges and since more power is usually required to produce a transition in the unfavourable case, one would naively expect the converse to be true: more dithering transitions in the unfavourable configuration than in the favourable.

The distribution of the transitions types as a function of the plasma current is shown in Fig.2. for the SND+ case. At high plasma current (I_p>400kA) direct transitions are mostly obtained while, around 350kA, the transitions occur in two steps with an intermediate dithering phase. In this figure both LD and DH transitions have been presented. Their slight misalignment is due to the fact that the plasma current still increases when the transition occurs, the latter usually happening when the divertor is being formed, which is done at the end of the plasma current ramp. Since these transitions are obtained in ohmic plasmas, this figure also shows that direct transitions are obtained when more power is injected into the

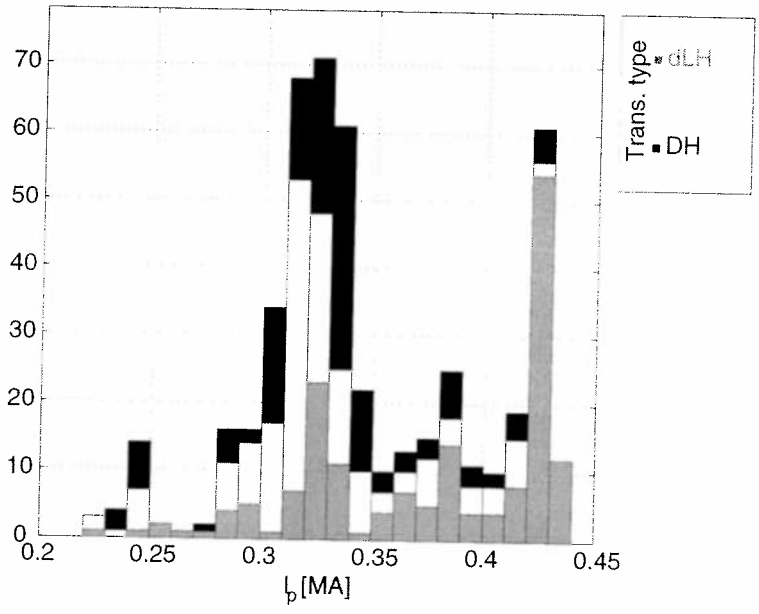

Figure 2: Distribution of the transition types along the plasma current axis. Grey (or pink): Direct LH transitions; light grey (green): LD transitions; dark grey (blue): DH transitions.

plasma. In the other configurations, similar distributions are observed against the plasma current. In the density domain, the distribution is slightly unbalanced, with more direct transitions occurring at high density. However this effect is due to the weak correlation between the plasma current and density. The plasma elongation has little effect on the distribution of the transition types. In contrast, the plasma triangularity does have an influence. At low triangularity (δ~0.35) most of the transitions are indirect while at higher triangularity (δ~0.55), more direct transitions are found in the SND+ case.

4. Synchronisation of LH transitions on the sawteeth cycle

It has already been reported that the heat pulse released at a sawtooth crash might help the triggering of an LH transition when arriving at the plasma edge. In order to identify whether sawteeth play a role in the LH transition process in TCV, a search for synchronisation has been undertaken following two approaches. The first one is based on a visual estimation of the synchronisation and is presented in the next subsection (4.1). The second approach (4.2) deals with the measured time delay between the LH transition and the crash of the preceding sawtooth.

In TCV, the sawtooth cycle sometimes shows a reduced crash followed by a ramp with normal slope and duration. The amount of energy released in the following crash is then much larger than average. Figure 3 shows an example of one of these so-called 'double sawtooth' events as seen on soft-X ray emission from the plasma centre. On the same figure, the D_α emission shows an LH transition occurring less than 1ms after the large sawtooth crash. These 'double sawteeth' are also identified in the two approaches presented in the next subsections and the synchronisation of the LH transition on the double sawteeth is jointly addressed.

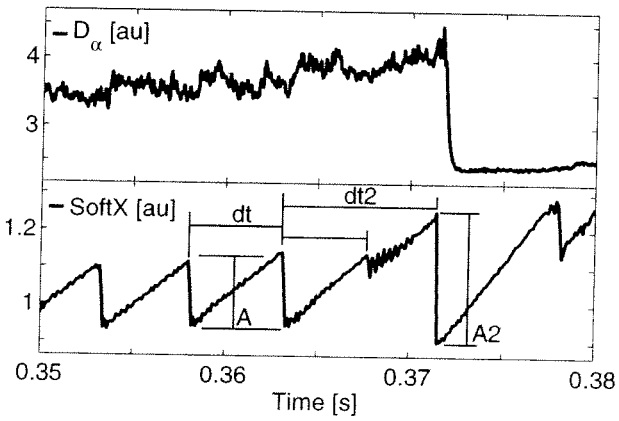

Figure 3: Time evolution of the D_α emission and soft-X ray emission from the plasma centre. The soft-X signal exhibits a double sawtooth and the LH transition is synchronised with the large double sawtooth crash. dt, dt2, A and A2 are used to determine the presence of a double sawtooth.

4.1 Synchronisation estimation through visual classification

The effect of sawteeth is visible on the D_α emission in

the form of a small increase in the emission at the time of the sawtooth crash, as shown in Fig.4, where the Soft-X ray emission of the plasma centre is plotted together with the D_α emission for three successive discharges. In these discharges, an abrupt drop in the D_α emission, indicating a direct LH transition, occurs after the beginning of such a small increase due to a sawtooth. A similar pattern is found in all three discharges even if they are slightly shifted in time, confirming the synchronisation of the two mechanisms. When this behaviour is found in any single discharge, it is considered as synchronised.

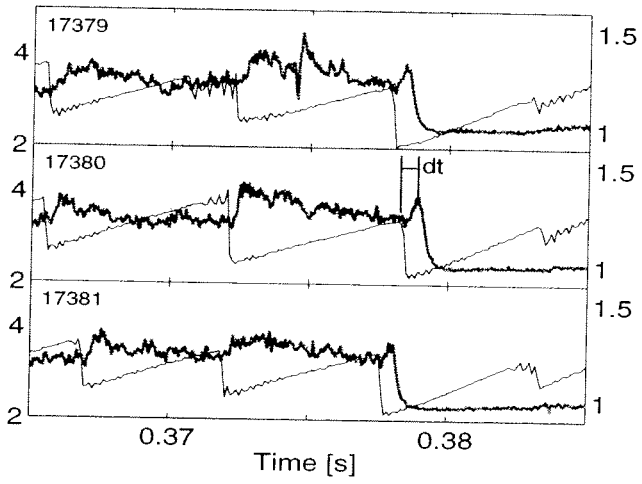

Figure 4: Evolution of D_α emission (thick line) and soft-X ray emission from the plasma centre (thin line) for three discharges showing the same pattern and same time interval between the sawtooth crash and LH transition, indicting the synchronisation of the two processes.

Another pattern which clearly indicates a synchronisation between the sawtooth cycle and the LH transition physics is shown in Fig.5. Here, the D_α emission pattern changes at each sawtooth crash, going from L-mode to high frequency dithering, then to low frequency dithering and finally to ELM free H-mode. In such a case, both LD and DH transitions are considered as synchronised with sawteeth.

An additional classification has been made for LH transitions occurring after a

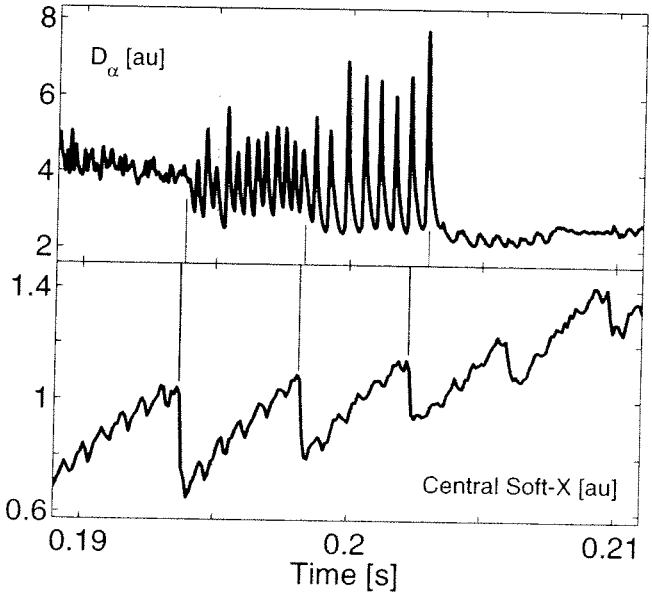

Figure 5: Evolution of D_α emission and soft-X ray emission from the plasma centre for a discharge with a dithering phase. The vertical lines show that a synchronisation exists between the sawteeth and the LH transition process.

	dLH	LD	DH
SND-	54 / **252** / *61*	1 / **13** / *1*	5 / **10** / *0*
SND+	16 / **78** / *74*	42 / **120** / *7*	62 / **82** / *5*
DND+	2 / **29** / *10*	3 / **77** / *1*	47 / **43** / *15*

Table 3: number of non-synchronised / **synchronised with a single sawtooth** / synchronised with a double sawtooth transitions for different plasma configuration and transition types

double sawtooth. A sawtooth is double when its crash amplitude and its duration exceed by a factor 1.5 the averaged values over the preceding 3 sawteeth, A2>1.5A, dt2>1.5dt in Fig.3. Moreover a strongly reduced sawtooth crash has to be present approximately at the time where the 1st sawtooth would have occurred.

All LH transitions in the database were tagged with the evaluation of the synchronisation, using these criteria. The distribution function of sawtooth synchronised LH transitions was then analysed for the different types of transitions and with respect to the operational domain.

Table 3 summarises the number of transitions that were non-synchronised, synchronised with a single sawtooth or synchronised with a double sawtooth, for each type of transition and plasma configuration.

This table shows that a large fraction of dLH and LD transitions are synchronised with either a single or a double sawtooth, independent of the plasma configuration. DH transitions are less sensitive to sawteeth, with only half of the transitions showing synchronisation. The ratio of the number of synchronised over non-synchronised dLH transitions slightly varies with the favourable/unfavourable ion ∇B drift direction. dLH transitions are more often synchronised with double sawteeth than other transitions. In the SND+ configuration almost half of the transitions are triggered by double sawteeth. In the DND+ configuration, a very large fraction of the dLH and LD transitions are synchronised with sawteeth.

In summary, the influence of the sawtooth cycle on the ohmic LH transitions is clearly established. This influence seems even stronger in the favourable ion ∇B drift case, for the dLH transition at least.

The distribution of the non-synchronised / synchronised transitions in the operational domain is quite uniform. The transitions following a double sawtooth are mostly found at the highest value of the plasma current (I_p~400kA). In these analyses, it would be interesting to know the statistical distribution of the double sawteeth in the operational domain, independently of the presence of the LH transitions. A more extensive analysis of the sawteeth properties should be performed but this remains beyond the scope of this paper.

4.2 Synchronisation estimation with the time delay statistics

The presence of synchronisation is also tested with the measurement of the time delay between the LH transition and the preceding sawtooth crash, indicated by 'dt' in Fig.3. The LH transition times are identified manually as the last moment before the drop in the D_α emission. The times of the sawtooth crashes are calculated from the Soft-X ray emission of the plasma core by a code which determines the beginning and the end of each sawtooth ramp. The time of a sawtooth crash is the average between the end of a ramp and the beginning of the next one. The identification of double sawteeth is also done automatically using the criteria described in the previous subsection.

The phase of the LH transition in the sawtooth cycle is easily calculated from the LH transition time, t_{LH}, and the previous and next sawteeth crash times, t_{stp} and t_{stn} respectively, using the expression $f_{st} = (t_{LH} - t_{stp}) / (t_{stn} - t_{stp})$ with $0<f_{st}<1$. This phase measure is more appropriate for estimating the presence of

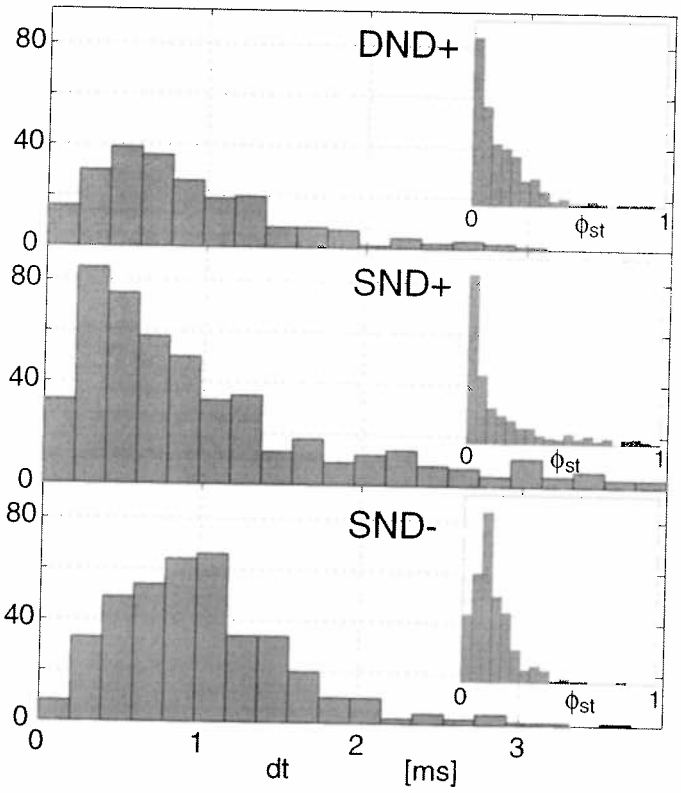

Figure 6: Distribution function of the time delays between the sawtooth and the LH transition for the different plasma configurations. Inserted: phase of the LH transition in the sawtooth cycle for the corresponding configurations.

any synchronisation, since it accounts for the full sawtooth cycle. However, the measure contains an error, smaller than 15%, due to the variation of the sawtooth period caused by the LH transition.

The distribution of the time intervals between the preceding sawtooth crash and the LH transition is shown in Fig.6 for the 3 configurations. All data points are used in this figure. Most LH transitions occur in the first 2ms after the sawtooth crash. The sawtooth period for these discharges ranges from 4 to 8ms. This strongly non-uniform distribution indicates that most LH transitions obtained in TCV are synchronised with sawteeth. Figures of the phase distribution of the LH transition in the sawtooth cycle are inserted in their respective boxes in Fig.6. These figures show that an important fraction of the LH transitions occur in the first 30% of the sawtooth cycle. This confirms the presence of synchronisation and, therefore, the strong influence of the sawteeth on the LH transition physics.

The heat pulse expelled at the sawtooth crash reaches the plasma edge in less than 0.2ms. Therefore the arrival of the heat pulse at the edge does not directly provide the trigger for the LH transition. An intermediate mechanism has to be invoked. This intermediate mechanism needs even more time to take place in the SND- configuration, as shown by the larger averaged delay in this configuration. The precise nature of the mechanism involved in the synchronisation is not yet known but the plasma current profile could play a role: the change in the pressure profile could lead to a change in the edge current profile and this mechanism needs some time to take place. A threshold value in the edge current could then be reached which leads to an LH transition.

The distribution function of the time delays for the 3 transition types is shown in Fig.7 for the SND+ case. Many direct LH transitions occur less than 0.5ms after the crash of the sawtooth in the plasma centre. The LD transitions occur slightly later on average, however synchronisation is still present. The DH transitions are

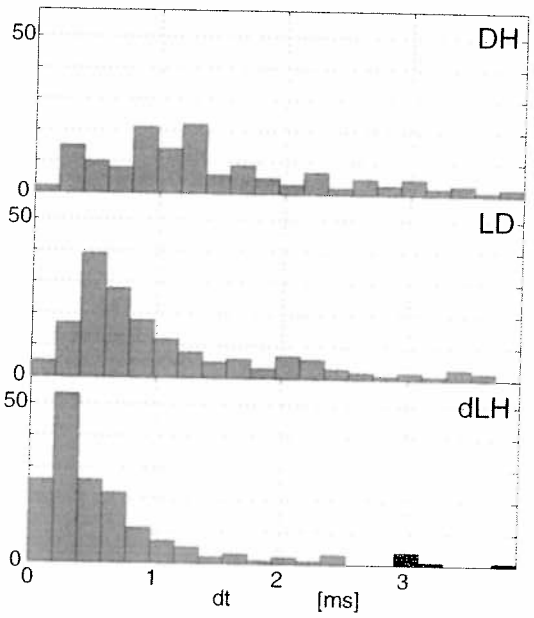

Figure 7: Distribution function of the time delays between the sawtooth and the LH transition for the different LH transition types, in the case of the SND+ configuration.

more widely distributed, indicating that this transition requires less influence from the sawtooth cycle.

Since most LH transitions are synchronised with sawteeth, the analysis of their distribution in the TCV operational domain has little interest.

5. Conclusion

All LH transitions obtained in TCV are considered in the search of synchronisation between sawteeth and LH transitions. First, the distribution in the operational domain of the type of transition is analysed. Direct LH transitions are preferentially found at high values of plasma current. The determination of the synchronisation is addressed following two approaches, one manual and one automatic. The manual approach is based on the visual classification of the synchronisation. This revealed that a large fraction of the LH transitions are synchronised with a sawtooth or a double sawtooth. In the SND- case the synchronisation seems slightly less clear. The automatic approach is based on the time delay between the transition and the last preceding sawtooth. The phase of the transition in the sawtooth cycle was estimated as well, and revealed that an even larger fraction of the LH transitions, almost all, are synchronised with a sawtooth crash. The difference in results between the two approaches resides in the fact that the time delay is large in the case of SND-. In the manual approach the synchronisation is not considered, while in the 2^{nd} approach, the calculated time delays shows a peaked distribution indicating the presence of synchronisation. The presence of a delay larger than the heat pulse transit time from the plasma centre to the edge indicates that a change in the plasma edge current, rather than pressure profile, could be responsible for the triggering of the LH transition.

Acknowledgement

The author would like to express its gratitude to the whole TCV team for its highly valuable work on the tokamak and its diagnostics. This work was partly supported by the Swiss National Science Foundation.

References

[1] T.Takizuka et al, this conference.

[2] T.N.Carlstrom et al. PPCF 40 (1998) 669

Control of electron Internal Transport Barriers on TCV

M.A. Henderson, R. Behn, S. Coda, I. Condrea, B.P. Duval, T.P. Goodman, A. Karpushov, Y. Martin, An. Martynov, J.-M. Moret, P. Nikkola, L. Porte, O. Sauter, A. Scarabosio, G. Zhuang and the TCV team

Centre de Recherches en Physique des Plasmas,
Association EURATOM - Confédération Suisse,
École Polytechnique Fédérale de Lausanne, CRPP - EPFL, 1015 Lausanne, Switzerland

Abstract. Current profile tailoring has been performed with the application of ECH and ECCD leading to improved energy confinement in the plasma core of the TCV tokamak. The improved confinement is characterized by a substantial enhancement (H-factor) of the global electron energy confinement time relative to the prediction of the RLW scaling law [1], which predicts well ohmic and standard ECH discharges on TCV. The improved confinement is attributed to a hollow current density profile producing a reversed shear profile creating an electron internal transport barrier. We relate the strength of the barrier to the depth of the hollow current density profile and the volume enclosed by the radial location of the peak current density. The ρ_T^* [2] criterion is used to evaluate the performance of the barrier relative to changes in the ECH parameters or the addition of ohmic current, which aid in identifying the control parameters available for improving either the strength or volume of the barrier for enhanced performance. A figure of merit for the global scaling factor is used which scales the confinement enhancement as the product of the barrier volume and strength.

PACS numbers: 52.25.Hi, 52.55.Fa, 52.55.Wq, 52.50.Sw

Submitted to: *Plasma Phys. Control. Fusion*

Control of electron Internal Transport Barriers on TCV

1. Introduction

Electron internal transport barriers (eITB) have been created on several fusion devices by applying heating off-axis [3, 4, 5]. These eITBs are typically generated during the current ramp up using off-axis deposition which inhibits the ohmic current from penetrating into the plasma center and facilitates the formation of a hollow current profile. This scenario is inherently transitory as the ohmic current eventually penetrates into the center, thus filling the hollow current density profile and destroying the eITB. By contrast, work performed in TCV for the past several years [6] has focused on the the generation of eITBs in stationary plasma conditions and maintaining the eITBs for several current redistribution time scales (τ_{CRT}, the time constant associated with the redistribution of the plasma current from the peaked to hollow current density profiles, typically $\sim 150ms$ for TCV). The eITBs have been formed and maintained with the plasma current driven non-inductively [7, 8] using a combination of electron cyclotron current drive (ECCD) and bootstrap current (BS) or inductively [9] with a non-zero ohmic current contribution ($I_\Omega \neq 0$). TCV's flexible high power electron cyclotron heating (ECH) system[10] generates very high central electron temperatures with $T_e >> T_i$, and has been used to study the eITB confinement dependence on the depositon location and current drive effects [11]. The confinement enhancement factors achieved approach $H_{RLW} \approx 6.0$ [12, 13]. The confinement is characterized by normalization to the RLW scaling law [1], *i.e.* $H_{RLW} = \tau_{eE}/\tau_{RLW}$, which well describes the confinement of L-mode plasmas in TCV[14] (in contrast to the ITER98-L mode scaling [15] which is not really appropriate when $T_e >> T_i$ and typically one-half τ_{RLW}).

This paper discusses the techniques for controlling the confinement enhancement of the eITB by modifying either the ECH or ECCD parameters or the magnitude of the inductive current. The confinement enhancement factor, H_{RLW}, is measured in stationary conditions. The second section describes the diagnostic tools which identify the existence of the eITB, and the techniques for controlling the confinement enhancement, which depends on the eITB's strength and volume. Where, the eITB strength is proportional to the depth of the hollow current density profile and the volume proportional to the radial location of the peak current density. Demonstration of the control of the barrier volume and strength in fully sustained non-inductively driven discharges ($eITB_{NI}$) is presented in the third section. The influence of the ohmic current in inductively driven discharges ($eITB_\Omega$) on the performance is described in section four. A global scaling law, which provides a figure of merit for the confinement enhancement, is proposed in section five followed by conclusions in section six.

2. The eITB basics

At present, there is no direct measurement of the local magnetic field line pitch angle on TCV. The improved confinement of the $eITB_{NI}$ discharges are attributed to a hollow current profile resulting in a reversed shear q-profile [16]. In [11] the strength of the barrier was related to q_o/q_{min} where q_o is the safety factor on axis and q_{min} is the minimum in the safety

factor while the volume is proportional to ρ^2_{qmin} (the radial position of q_{min}). Here q_o, q_{min} and ρ_{qmin} were obtained from simulations of the plasma current density profiles during stationary plasma conditions in $eITB_{NI}$. I_{BS} was derived from the electron pressure profiles, P_e[17] and the ECCD profile from coupled Fokker-Planck ray tracing calculations including cross field transport [16, 18]. The H_{RLW} of the $eITB_{NI}$ was also shown to be linearly dependent on the product of the barrier strength and volume.

It is convenient to characterize the barrier strength as depending on the depth of the hollow current density profile or $(J_{max} - J_0)/J_{max}$, where J_{max} is the maximum plasma current density and J_0 is the current density on axis, and by the volume enclosed by the barrier, or $\rho^2_{J_{max}}$, the radial location of J_{max}. Improving the confinement can be accomplished by increasing the depth and/or the width of the hollow current density profile. In contrast, the confinement can be degraded by adding current in the center (decreasing the depth) or narrowing the current density profile (reducing the volume). The hollow current density profile in the $eITB_{NI}$ forms from a large bootstrap current of up to 70% of the total plasma current[7]. Generating more bootstrap current increases the depth of the hollow current density profile, while generating bootstrap current further off-axis increases the width of the hollow current density profile. The bootstrap current depends upon the electon pressure gradient (∇P_e), which is experimentally seen to be dominated by the temperature rather than the density gradient. This connection motivates an alternative approach for evaluating the performance of the eITBs using the $\rho^\star_T$ parameter [2] defined as:

$$\rho^\star_T(R,t) = \rho_s(R,t)/L_{Te}(R,t)$$

where $L_{Te} = -T_e/(\partial T_e/\partial R)$ is the local temperature gradient scale length, T_e the electron temperature, R the major radius on the equatorial plane, $\rho_s = c_s/\omega_{ci}$ the ion Larmor radius at the sound speed, c_s the sound speed with T_e and ω_{ci} the ion cyclotron frequency. The barrier strength and volume is related to $\rho^\star_T$ since the bootstrap current, which creates the hollow current density profile, is dominated by ∇T_e. An example of the T_e and $\rho^\star_T$ profiles averaged over four phases of a discharge is shown in figure 1. Phase **A** corresponds to the ohmic target plasma, **B** the co-ECCD off-axis preheat phase, **C** same conditions as **B** but with a weak eITB (no central heating) and **D** centrally heated eITB. The maximum in $\rho^\star_T$ ($\rho^\star_{max}$) can be correlated to the strength of the barrier, with a threshold for eITB existence when $\rho^\star_{max}$ exceeds $\approx$ 0.04. The radial position of $\rho^\star_{max}$ ($\rho_{\rho^\star}$) can be correlated to the volume enclosed by the barrier. Both $\rho^\star_{max}$ and $\rho_{\rho^\star}$ are obtained from the measured T_e profiles and can quantify the eITB confinement enhancement even in transitory scenarios, in contrast to the cumbersome simulations required for obtaining q_o, q_{min} and ρ_{qmin}.

An example of the relationship between the T_e profiles and the $eITB_{NI}$ performance is given in figure 2. In Cycle S_+ central heating is added to an eITB which increases the central T_e without broadening the profile. The plasma responds with an increase in P_e and ∇P_e generating more bootstrap current which increases J_{max} effectively deepening the hollow current density profile, thus strengthening the barrier. This sets up a positive feedback, the

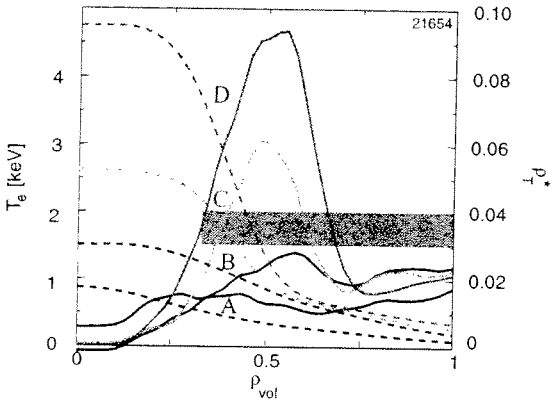

Figure 1. *T_e (dashed) and ρ^* (solid) profiles averaged during four phases of an eITB discharge. Phase* **A** *during the stationary ohmic phase.* **B** *during the P_{co} pre-eITB.* **C** *during the eITB without central heating and* **D** *during the centrally heated phase.*

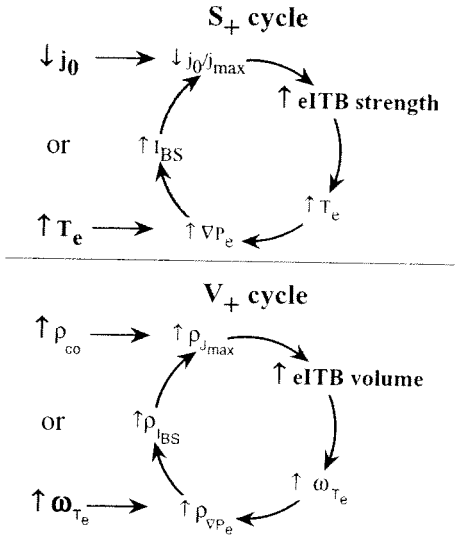

Figure 2. *Illustration of the plasma response to either a rise in T_e (cycle* **S***) or a broadening of the T_e profile (cycle* **V***). A positive feedback is established with strengthening or broadening of the eITB which further increases or broadens the T_e profile until an equilibrium is established.*

stronger barrier increasing the central temperature leading to an even stronger barrier. The cycle continues until the eITB reaches some equilibrium scenario determined by the plasma and heating parameters or the profiles become too peaked resulting in a degradation in performance due to the onset of an ideal MHD mode. The cycle can be reversed, S_- with a decrease in T_e reaching an ultimate equilibrium with a decrease in barrier strength. Note the '+' and '-' subscript on 'S' refers to the forward and reverse direction of the cycle.

In Cycle V_+, the central heating is kept constant but the T_e profile is broadened (ω_{T_e}). The plasma responds with an increase in the radial position of the pressure gradient, $\rho_{\nabla P_e}$, the radial location of the bootstrap current profile, $\rho_{I_{BS}}$, moves outward increasing the width of the hollow current density profile, $2\rho_{I_{max}}$, thus enlargening the barrier volume. Positive feedback occurs with the increase in the volume of the barrier which broadens the T_e profile eventually further increasing the volume until some equilibrium is reached. This cycle can also be reversed, V_- with a narrowing of the temperature profile shrinking the volume of the hollow current profile.

In reality the eITB dynamics are more complicated than portrayed in the above illustrations. For example, mechanisms used to modify the temperature profile can also provide a local current source setting up either of the positive (or negative) feedback cycles starting with direct modifications to the the I_P profile. The mechanisms for modifying the T_e and I_P profiles investigated in this paper include: off-axis co-ECCD power (P_{co}) and deposition location (ρ_{co}), central ECCD

power (P_o) and toroidal injection angle (ϕ_o), and inductively driven current (I_Ω).

3. Control of the $eITB_{NI}$

Scans of ϕ_o and ρ_{co} have been performed on a shot-to-shot basis in $eITB_{NI}$ with $P_o = 0.5MW$, $P_{co} = 0.9MW$ and typical plasma parameters $I_P \approx 80kA$, $n_{el} \approx 0.7x10^{19}m^{-3}$ (line average electron density), $\kappa \approx 1.5$ (elongation). While keeping the $\rho_{co} \approx 0.4$, ϕ_o was scanned from +5 (co-ECCD) to -5 (cnt-ECCD). A noticeable increase in T_e and ρ_T^* is observed as ϕ_o progresses toward cnt-ECCD while the foot of the T_e profiles remain fairly constant, $\rho \approx 0.5$, as shown in figure 3a. The injection of cnt-ECCD on-axis provides a negative current source in the center of the plasma which increases the depth of the hollow current density profile and increases H_{RLW}, see figure 3b. Increasing the depth should strengthen the eITB, i.e. establish a S_+ cycle characterized by an increase in central T_e, bootstrap current (I_{BS}) and ρ_{max}^* while maintaining $\rho_{\rho*}$ constant. Indeed, I_{BS} increases, see figure 3b, which results in a net increase in I_P despite the decrease in the overall EC current drive (I_{CD}) with $\phi_o < 0$. The barrier strength, ρ_{max}^*, increases while the barrier volume, $\rho_{\rho*}$, increases only slightly, see figure 3c. The slight increase in the barrier volume can be attributed to a second order effect on the increase in I_{BS}. Since the I_{CD} profile is nearly flat due to current diffusion[16], an increase in I_{BS} while decreasing I_{CD} will slightly displace J_{max} outward setting up a V_+ cycle increasing the barrier volume.

A scan of the radial location of the off-axis co-ECCD deposition location was performed while maintaining central heating with no toroidal injection (ECH). As the deposition moves outward in ρ_{co}, the J_P and T_e profiles broaden, which increases the volume of the barrier, initiating the V_+ cycle. However, as ρ_{co} increases, the EC current drive efficiency decreases due to lower electron temperatures off axis resulting in a decrease in J_{CD}. The

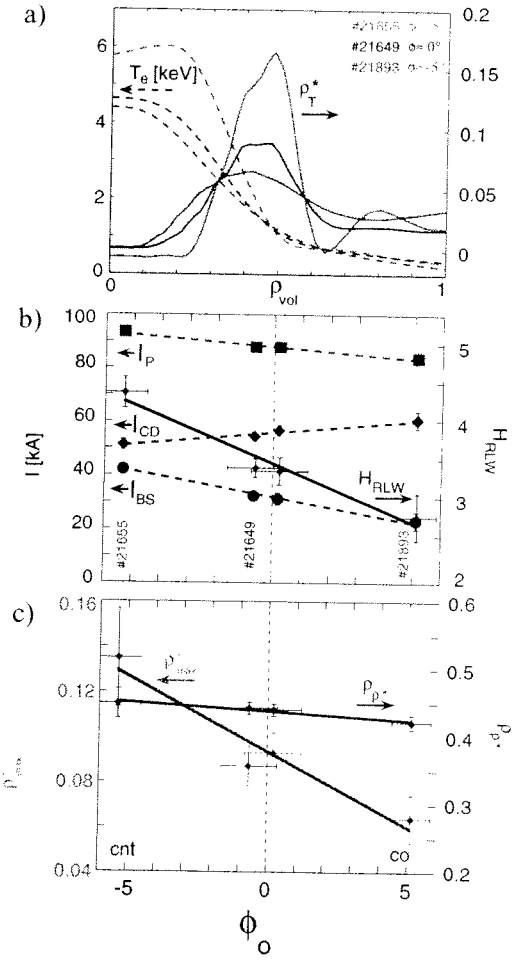

Figure 3. *The $eITB_{NI}$ performance during a scan of the toroidal injection angle, ϕ_o as observed on (a) the T_e (dashed) and ρ_T^* (solid) profiles; (b) the enhancement factor, H_{RLW} (solid), I_P, I_{CD} and I_{BS} (dashed); and (c) the barrier strength and radius.*

reduction in J_{CD} decreases both J_o and J_{max} due to diffusion, while the depth of the hollow current density profile ($J_{max} - J_o)/J_{max}$) increases, resulting in a stronger barrier, or a S_+ cycle. Thus increasing ρ_{co} should set in motion both V_+ and S_+ processes, which is evidenced in a wider and higher T_e profile (as shown in figure 4a), and an increase in the bootstrap current (see figure 4b). Also, both the barrier volume, $\rho_{\rho*}$, and strength, ρ^*_{max}, increases as shown in figure 4c.

There exists a potential for independent control of either the barrier volume or strength using both ρ_{co} and ϕ_o. For example, the eITB strength can be increased while maintaining constant eITB volume by adding cnt-ECCD on axis with only a slight decrease of ρ_{co}. Conversely, the eITB volume can be enlarged while maintaining constant strength by increasing ρ_{co} and then adding co-ECCD centrally to degrade the eITB strength.

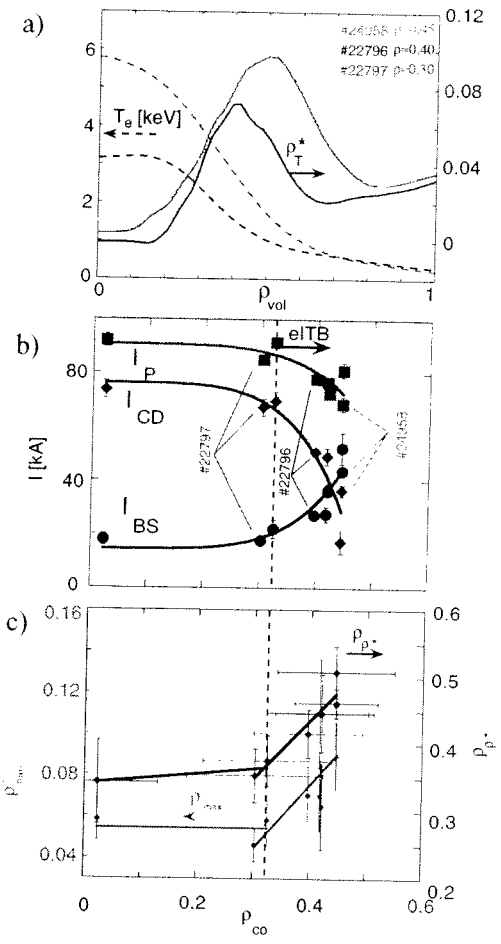

Figure 4. *The $eITB_{NI}$ performance during a scan of the radial deposition, ρ_{co} as observed on (a) the T_e (dashed) and ρ^*_T (solied) profiles: (b) I_P, I_{CD} and I_{BS}: and (c) the barrier strength and radius.*

4. Inductive current influence on the eITB

Since the current driven inductively is proportional to $T_e^{3/2}$, any ohmic current induced in an eITB will be predominately deposited in the center of the plasma. The hollow current density profile will be partially filled by a positive loop voltage driving an additional central current source, which weakens the barrier. Also, the current profile will be narrower decreasing ρ_{jmax} and decreasing the volume of the barrier. The eITB performance should degrade with both S_- and V_- cycles as portrayed in figure 2. This process is demonstrated by comparing an $eITB_{NI}$ ($\phi_o = 0$) used in figure 3b with an $eITB_\Omega$ (equivalent EC conditions) with $I_\Omega \neq 0$, but with $I_\Omega < I_{BS}$. As shown in figure 5 the T_e profiles decrease and are narrower with the addition of ohmic current (green curve) relative to the $eITB_{NI}$ (blue curve). Also the barrier strength and volume decrease as expected with the shrinking and filling in the hollow current density profile. If I_Ω is sufficently large relative to I_{CD} and I_{BS}, the current hole could be filled and the $eITB_\Omega$

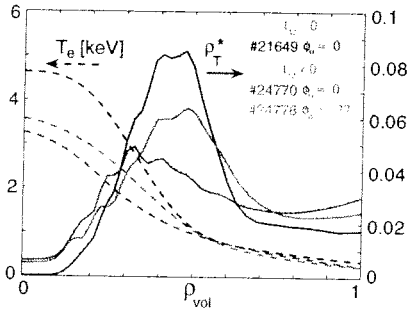

Figure 5. *The T_e (dashed) and ρ_T^* (solid) profiles for an $eITB_{NI}$ (blue curves) and equivalent $eITB_\Omega$ with degraded performance due to $I_\Omega \neq 0$ (green curve) with central ECH. The $eITB_\Omega$ is repeated with cnt-ECCD on-axis to negate I_Ω (red curve)*

entirely destroyed.

The additional ohmic current in the center of the plasma can be cancelled out using counter ECCD on axis ($\phi_o < 0$). The $eITB_\Omega$ discharge described in figure 5 (green curve) was repeated, but with cnt-ECCD on-axis $\phi_o = -27$ (red curve). The barrier volume and strength improve with cnt-ECCD as seen in the ρ_T^* profiles, the degradation associated with the addition of I_Ω is eliminated. However, the same confinement enhancement achieved in the $eITB_{NI}$ (green curve) is not obtained, an increase in P_o beyond 0.5MW would be required. Typically, more counter ECCD is needed on axis for negating the central ohmic current as $[I_P - (I_{BS} + I_{co})]$ increases. For the $eITB_\Omega$s obtained on TCV, P_o ranges from 0.7 to 2.0MW (versus 0.5MW for $eITB_{NI}$ studied). Note that the $eITB_\Omega$ requires less power off-axis, since only broadening of the T_e and current density profiles is required rather than fully sustaining the plasma current as in the case of $eITB_{NI}$. The cnt-ECCD becomes nearly essential for creating the hollow current density profile as $I_\Omega > I_{CD} + I_{BS}$.

The cnt-ECCD does not only provide a negative current source, but also heats the plasma. There is a feedback loop on the dI_{OH}/dt to maintain I_P constant. The plasma conductivity increases with the increase in T_e, the loop voltage decreases even though I_Ω increases to compensate I_{cnt} and maintain I_P constant. Small variations in measured central T_e lead to a large range of calculated central ohmic and cnt-ECCD driven current densities and a large variation in the simulated values of q_{min}, q_o and ρ_{q-min}.

An additional example has been shown in discharge #24913 which was reported in [12, 13]. An eITB is obtained with the plasma current fully sustained noninductively, and then ohmic current is added by a pre-programmed ramp in the ohmic transformer current. The addition of the ohmic current degrades the eITB performance by filling in and decreasing the hollow current density profile resulting in a decrease in barrier strength and volume.

5. global scaling

In reference [11] a general figure of merit for the enhancement confinement was proposed which demonstrated a linear increase in H_{RLW} as a dependence of the product between the eITB volume (ρ_{q-min}^2) and the eITB strength (q_0/q_{min}). The inclusion of $eITB_\Omega$ plasmas could not be accomplished due to the inaccuracies in simulating the ohmic and cnt-ECCD current density contributions as described above. The enhancement figure of merit has been reproduced characterizing the eITB's using ρ_T^*, with the eITB volume and strength represented by ρ_{max}^* and

$\rho_{\rho*}$ [13]. Recently the number of ohmic discharges included in the database has been increased and reveals a potential improved scaling of $eITB_\Omega$ (red points) over $eITB_{NI}$ (blue points) as shown in figure 6. This seems to be in contrast with the conclusion drawn in the previous section, that the ohmic current fills in the hollow current profile degrading the eITB. The previous comparison was performed with all eITB's formed with $P_{co} = 0.9MW$ and $P_o = 0.45MW$. In $eITB_\Omega$ the ratio P_o/P_{co} has been increased to at least 3.0 which permits more power to be deposited within the barrier for more effective heating of the eITB, where P_o is the sum of both the injected power from cnt-ECCD and the ohmic contribution. Past experiments have demonstrated that when P_o increases, τ_{eE} remains constant or slightly increases resulting in a significant increase in H_{RLW} (in contrast to L-mode discharges where τ_{RLW} scales as $P^{-0.5}$). The power deposited off-axis although required for forming the eITB contributes minimally to heating inside the barrier. Future experiments are planned to test the confinement enhancement factor for different P_o/P_{co} power ratios and search for an optimum relative to the plasma parameters, such as current, density, elongation, etc.

The product ρ^*_{max} and $\rho^2_{\rho*}$ is a simple figure of merit for the enhancement factor of these steady state eITB's and suggests the possibilty of even further enhancement as the barriers are extended in volume and strength.

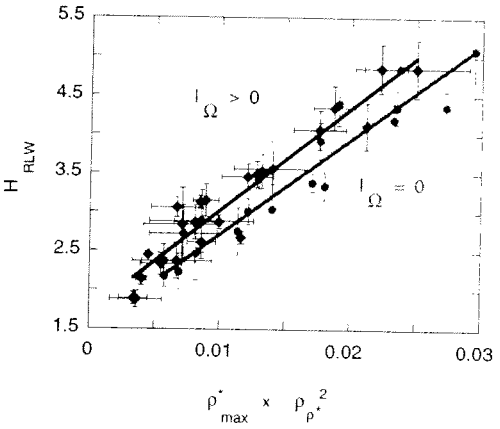

Figure 6. *A figure of merit of the $eITB_\Omega$ (blue) and $eITB_{NI}$ (red) is given as the product of the barrier strength and volume ($\rho^*_{max}\ \rho_{rho*}$).*

6. Conclusions

The ρ^*_T profiles have been used to characterize the confinement performance of both fully sustained and inductively driven eITBs. The eITB is believed to be associated with a hollow current density profile with the barrier strength related to the depth and barrier volume related to the width of the hollow region. The barrier strength is defined as the maximum in ρ^*_T (ρ^*_{max}), while the barrier volume is dependent on the radial location of this maximum ($\rho_{\rho*}$). The influence of the toroidal injection angle on-axis (ϕ_o) and the off-axis radial position (ρ_{co}) on the confinement enhancement has been characterized pointing the way to possible individual control of either the strength or volume.

The influence of additional ohmic current (I_Ω) to the above eITBs has been shown to degrade the confinement by reducing the barrier strength and volume with the use of ρ^*_{max} and $\rho_{\rho*}$. This degradation can be reversed with additional

counter-ECCD in the center. The performance of fully sustained and inductively driven eITBs have been compared in one global figure of merit equal to the product of the barrier strength and volume. Slight variations in the figure of merit may be attributed to different P_o/P_{co} power ratios, the ratio of power injected centrally versus off-axis. The power on-axis is more efficient in optimizing the performance of the barrier.

7. Acknowledgements

The authors would like to thank the many individuals who operated TCV and diagnostics, which allowed the experiments to occur. Without their participation these results would not have existed, in particular thanks goes to A. Degeling, D. Fasel, P.F. Isoz, A. Perez, R. Pitts, U. Siravo, G. Tonetti and H. Weisen. A special thanks to Xavier Llobet for his continued patience in taming the complexities of our plant control and data acquisition systems on a daily basis.

This work was supported in part by the Swiss National Science Foundation.

references

[1] P.H. Rebut, P.P. Lallia, and M.L. Watkins, in Porceedings of the 12th International Conference of Plasma Physsics and Controlled Fusion Reasearch, Nice, 1988 (IAEA, Vienna, 1989), Vol. 2 p.191.

[2] G. Tresset, X. Litaudon, D. Moreau *et al*, Nucl. Fusion **42** (2002) 520.

[3] G.M.D. Hogeweij *et al*, Plasma Phys. Contr. Fus. **44** (2002) 1155 and ref therein.

[4] S. Ide *et al*, Plasma Phys. Contr. Fus. **44** (2002) A137.

[5] A.K.A. Razumova *et al*, Plasma Phys. Contr. Fus. **42** (2000) 973 and ref therein.

[6] S. Coda, Plasma Phys. Contr. Fus. **42** (2000) B311.

[7] O. Sauter *et al*, Proc. 29th EPS Conf. on Controlled Fusion and Plasma Physics (Montreux, 2002), Europhysics Conf. Abstr. **26B** (2002) P2-087.

[8] T.P. Goodman *et al*, *ibidem*. P2-081.

[9] Z.A. Pietrzyk *et al*, Phys. Rev. Lett. **86** (2001) 1530.

[10] T.P. Goodman, S. Alberti, M.A. Henderson, A. Pochelon and M.Q. Tran in *Proceedings of the* 19^{th} *Symposium on Fusion Technology* (Lisbon, 1996), Elsevier, Amsterdam (1997) 565.

[11] M.A. Henderson, S. Alberti, C. Angioni *et al*, Phys. of Plasmas vol. **10** no. 5 (2003) 1796.

[12] R. Behn *et al*, Proc. 30th EPS Conf. on Controlled Fusion and Plasma Physics (St. Petersbourgh, 2003), Europhysics Conf. Abstr. **27A** (2003) P3-208.

[13] Y. Martin, M.A. Henderson, S.Alberti *et al*, Proc. 30th EPS Conf. on Controlled Fusion and Plasma Physics (St. Petersbourgh, 2003), Europhysics Conf. Abstr. **27B** (2003) , Nucl. Fusion (accepted for publication).

[14] A. Pochelon, T.P. Goodman, M.A. Henderson *et al*, Nucl. Fusion **39** (1999) 1807.

[15] ITER PHYSICS BASIS, chapter 2, Nucl. Fusion **39** (1999) 2175.

[16] P. Nikkola, O. Sauter, R. Behn *et al*, Proc. of the 12^{th} Joint Workshop on ECE and ECRH, May 13-16, 2002, Aix-en-Provence, (World Scientific, Singapore, 2003) 257: *"Modeling of the Electron Cyclotron Current Drive experiments in the TCV tokamak"*, Nucl. Fusion (*accepted for publication*).

[17] O. Sauter, C. Angioni and Y,R, Lin-Liu Phys. Plasmas **6**, 2834 (1999); **9**, 5140 (2002).

[18] R.W. Harvey and M.G. McCoy in *Proceedings of the IAEA Technical Committee Meeting on Numerical Modeling of Plasmas, Montreal*, 1992 (IAEA, Vienna, 1993).

Roles of aspect ratio, absolute B and effective Z for the H-mode power threshold in tokamaks of ITPA database

ITPA H-mode Power Threshold Database Working Group# presented by T Takizuka*

*Japan Atomic Energy Research Institute, Naka Fusion Research Establishment, Naka-machi, Naka-gun, Ibaraki-ken 311-0193, Japan

Received

Abstract. Analysis of ITPA H-mode power threshold database is advanced to study roles of aspect ratio A, absolute magnetic field and effective charge number Z_{eff}. A new scaling expression for power threshold P_{thr} is presented. Absolute B at the outer surface is used instead of B_t in the scaling, and the I_p dependence of P_{thr} in low-A tokamak is described without the explicit use of I_p variable. Clear and strong dependence on Z_{eff} is found; $P_{thr} \propto Z_{eff}^{0.7}$. Both the scattering nature in the data fitting and the "low-density anomaly" can be reduced. Nonlinear A dependence is also suggested. The P_{thr} in ITER is predicted on the basis of the present scaling.

1. Introduction

H-mode operation is considered suitable for tokamak fusion reactors, such as ITER [1], because of its high confinement performance. The H-mode state is achieved with the heating power above a certain threshold P_{thr}. To evaluate the additional heating power necessary for entering the H-mode state in a future reactor and to find its operation point, a quantitative formula of P_{thr} is required. Since such a theoretical formula has not been developed so far [2], empirical formulas have been proposed among which scaling expressions based on the ITPA (International Tokamak Physics Activity) threshold database are the most reliable [3,4,5].

It has been found that these expressions for P_{thr} include a small number of parameters; toroidal magnetic field B_t, line averaged electron density n_e, and plasma surface area S (or major radius R and minor radius a). The P_{thr} correlates strongly and positively with both B_t and n_e. The R^2 dependece in an early scaling, $P_{thr} \sim B_t n_e^{0.75} R^2$ [3], has been modified to the S dependence by the later analysis of the extended database [4]. Several expressions were shown there and they can be approximated as

$$P_{thr0} = 0.06\, B_t^{0.7} n_{20}^{0.7} S^{0.9} \qquad (1)$$

with an uncertainty of $G = (B_t/3)^{\pm 0.1} (n_{20}/0.6)^{\pm 0.1} (S/60)^{\pm 0.1} (3a/R)^{\pm 0.2}$. In the present paper, we

Alcator C-Mod: J A Snipes, M Greenwald; ASDEX/ASDEX Upgrade: F Ryter, O J W F Kardaun, J Stober; COMPASS-D/MAST: M Valovic; DIII-D: T N Carlstrom, J C DeBoo; JET/EFDA: Y Andrew, J G Cordey, R Sartori, K Thomsen; JFT-2M/JT-60U: T Takizuka, Y Miura, T Fukuda, Y Kamada, K Shinohara, K Tsuzuki; PBX-M/NSTX: S M Kaye, C Bush, R Maingi; TCV: Y Martin; TUMAN-3M: S Lebedev;

employ the units as P in MW, B in T, n_{20} in $10^{20}m^{-3}$, R in m, a in m, and S in m^2. One of the recent fitting formulas, $P_{thr} = 0.042\ B_t^{0.78} n_{20}^{0.64} S^{0.94}$ [5], is laid surely within this uncertainty. The above simple fitting formula (1) is used as a normalizing basis in the following analysis.

Recently data from spherical tokamaks (MAST [6] and NSTX [7]) were supplied to the ITPA database and the range in the aspect ratio A ($\equiv R/a$) was significantly extended [5]; $6.2 > A > 2.4$ (standard tokamaks), $A \approx 1.45$ (MAST) and $A \approx 1.32$ (NSTX). Now the database includes Alcator C-Mod, ASDEX, ASDEX Upgrade, COMPASS-D, DIII-D, JET, JFT-2M, JT-60U, MAST, NSTX, PBX-M, TCV, and TUMAN-3M. A new analysis has been started to find the cause of large residual scatter in the experimental data when compared to above scaling expressions. It was pointed out in [5] that one of the major causes is the effective charge number Z_{eff}. In this paper, we advance the analysis from the previous works by aiming to study the roles of A and Z_{eff} on the H-mode power threshold.

2. Data selection

2.1 Phase and heating method

When we analyze the database to develop a scaling, we should be careful how to select the data points. In the present work we treat the data at the LH transition phase. The dithering phase is supposed to be a combined phase of L- and H- modes, and the data points related to this phase are used in the analysis.

As for the heating method, we do not adopt any restriction. We have not observed any significant difference in P_{thr} among NB (neutral beam) heating, IC (ion cyclotron) heating, EC (electron cyclotron) heating, Ohmic heating, and the combined heating with them.

2.2 Configuration

Positions of null points relative to the direction of ion grad-B drift affect the L-H transition. Usually the power threshold is smaller in the single null (SN) configuration for the drift direction towards the null point (IGRADB = 1) than that for the opposite drift direction (IGRADB = -1). In the double-null (DN) configuration (IGRADB = 0), the P_{thr} looks not increasing much compared with that for IGRADB = 1. Therefore, in the following analysis, we use the data of IGRADB = 0 and 1. This evaluation is justified by figure 1 showing the

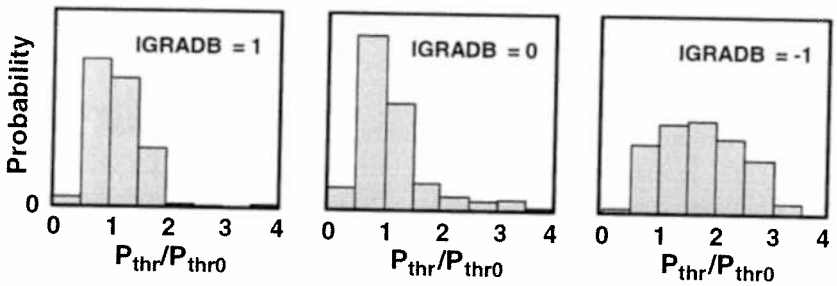

Figure 1. Distribution function of P_{thr}/P_{thr0} in JET. Power threshold for IGRADB = -1 is larger than that for IGRADB = 0 and 1.

distribution function of P_{thr}/P_{thr0} for different configurations in JET (Criterions described below are imposed).

2.3 Ion mass number

The L-H transition occurs easily at a lower heating power in deuterium discharges than in hydrogen discharges. It has been found from JET data that the threshold power is reduced in tritium discharges. The dependence of P_{thr} on the ion mass number M was roughly given as an inverse proportion; $P_{thr} \propto 1/M$ [8]. In the following analysis, we only use data of $M_{eff} = 1.5$ and 2 by assuming both data being $M = 2$ data, where $M_{eff} = (M_{plasma}+M_{beam})/2$ is the effective mass number. The data of $M_{eff} = 1.5$ correspond to discharges for hydrogen beam into deuterium plasma, and such plasmas at the L-H transition time consist mainly of deuterium.

2.4 Low density and low safety factor

In low-density plasmas, recycling neutral particles from the divertor region penetrate deeply into the core plasma. The penetration length for neutral deuterium with energy of ~10 eV is about $L_{pen} \sim (0.01/n_{20})$ m. The deep penetration of neutrals can affect the L-H transition. Therefore we use the data satisfying a condition $L_{pen}/(\kappa a) < 0.1$, i.e., $(n_{20}\kappa a) > 0.1$. By this criterion TUMAN-3M data ($n_{20}\kappa a \sim 0.03$ and $P_{thr}/P_{thr0} \sim 5.5$) and low-density COMPASS-D data ($n_{20}\kappa a \sim 0.02$ and $P_{thr}/P_{thr0} \sim 12$) are omitted, whose P_{thr} values are extremely higher than P_{thr0}. The selection window for the density is wider than that applied to the previous analyses in [4,5], and the "low-density anomaly" with the relation to Z_{eff} is investigated in section 4.

Power threshold tends to increase gradually when the safety factor near the plasma surface q_{95} (95% flux surface) decreases below 2.5. This tendency is clearly found in TCV data. Therefore we use the data of $q_{95} > 2.5$.

The total data selected under the above restrictions (subsections 2.1-2.4) are distributed against the values of $\ln(P_{thr}/P_{thr0})$ almost in a Gaussian form with the standard deviation $\sigma \sim 0.36$.

3. Power threshold in low-A tokamaks and role of absolute B

Power threshold in low-A tokamaks is rather large compared with above scaling expressions derived by using the data of standard tokamaks ($2.4 < A < 6.2$). The ratio P_{thr}/P_{thr0} is about 1.6 for MAST data ($A \approx 1.45$) and about 3.7 for NSTX data ($A \approx 1.32$). It is noted that the MAST data are of Ohmic heating and DN configuration (IGRADB = 0), while the NSTX data are of NB heating and SN configuration with the favorable drift direction (IGRADB = 1). It has been emphasized that P_{thr} in NSTX depends strongly and positively on the plasma current I_p [7] contrary to the above P_{thr} scalings with weak I_p dependence.

These different features can be explained in principle by introducing the absolute magnetic field to the analysis. We consider the absolute B at the outer mid-plane of the plasma surface because this region is supposed important for the L-H transition. The absolute B is given as $|B|_{out} = (B_{tout}^2 + B_{pout}^2)^{0.5}$, where $B_{tout} = B_t \times A/(A+1)$ and $B_{pout} = (\mu_0 I_p/2\pi a) \times (1+A^{-1})$. Several approximations are used to estimate the poloidal field at the outer mid-plane B_{pout}, e.g., the poloidal-field asymmetry coefficient $A \approx 1$. We replace B_t with $|B|_{out}$ and correct the coefficient from 0.06 to 0.072 in equation (1) and obtain a new basis scaling;

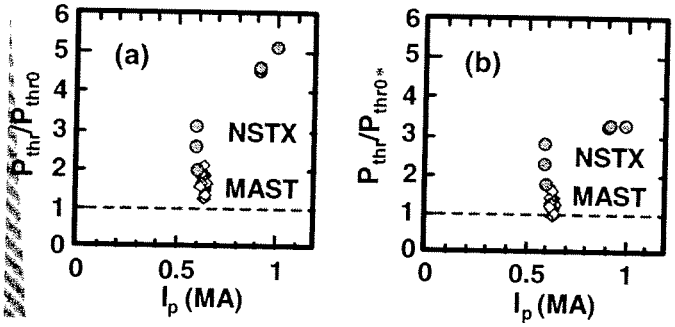

Figure 2. Dependence of the ratio P_{thr}/P_{thr0} and P_{thr}/P_{thr0*} on I_p for low-A tokamaks (MAST and NSTX).

$$P_{thr0*} = 0.072\,|B|_{out}^{0.7} n_{20}^{0.7} S^{0.9} \qquad (2)$$

Figure 2 shows (a) P_{thr}/P_{thr0} and (b) P_{thr}/P_{thr0*} for MAST and NSTX. One can clearly see that the I_p dependence of the P_{thr}/P_{thr0*} becomes very weak. The resulting scaling expression subsumes the I_p dependence at low aspect ratio and is consistent with the full set of data without any explicit I_p dependence. In addition, the ratio P_{thr}/P_{thr0*} is remarkably reduced from the value of P_{thr}/P_{thr0} to 1.25 for MAST and 2.8 for NSTX, but still stays above unity. We study further the role of A in section 5.

4. Role of Z_{eff}

The store of Z_{eff} in the database is rather poor. In the present version (September 2003), Z_{eff} data from ASDEX, DIII-D, Alcator C-Mod, JET, JT-60U and NSTX are stored, and those from ASDEX Upgrade were supplied very recently. For ASDEX and Alcator C-Mod, data points with Z_{eff} are limited. Measured values of Z_{eff} sometimes contain large error bars. Under such situation, the Z_{eff} dependence has not been shown in P_{thr} scaling expressions.

In order to estimate the accuracy of Z_{eff} values, we compare the measured Z_{eff} with the calculated values given by $Z_{eff,cal} \propto V_{surf} S_{cross} T_{eff}^{1.5}/(2\pi R I_p)$. We make a data subset within $Z_{eff}/Z_{eff,cal} = e^{0\pm0.5} \times \langle Z_{eff}/Z_{eff,cal}\rangle_{tok}$, which is used to develop a P_{thr} scaling including Z_{eff}. Here V_{surf} is the one-turn surface voltage, S_{cross} is the plasma cross-sectional area (or $\pi\kappa a^2$), $T_{eff} = W/3n_eV$ is the effective temperature (W: plasma stored energy, V: plasma volume), and $\langle\ \rangle_{tok}$ represents the average against a single tokamak. Though the data of Alcator C-Mod with Z_{eff} are the data of IGRADB = -1 (see subsection 2.2), these data are used in the analysis here. The data of JET reveal quite large scattering nature especially for IC and combined NBIC heating cases. The reason why P_{thr} in JET become sometimes much larger than P_{thr0} has not been clarified so far. For the simplicity of the analysis here, we use only JET data for NB heating.

Figure 3(a) shows the dependence of P_{thr}/P_{thr0} on Z_{eff} for JT-60U, where solid circles are the data inside a density window ($0.19 < n_{20} < 0.26$). We see the clear Z_{eff} dependence of $P_{thr}/P_{thr0} \sim Z_{eff}^{0.80}$ inside the n_e window and similarly $\sim Z_{eff}^{0.60}$ for all JT-60U data. The Z_{eff} generally increases with the decrease of n_e as shown in figure 3(b). Even though the Z_{eff} and n_e relate with each other, the Z_{eff} dependence of P_{thr}/P_{thr0} seems unified; $P_{thr}/P_{thr0} \propto Z_{eff}^{\alpha}$ with $\alpha \approx 0.7$. The data other than JT-60U have similar dependence though the scattering are rather large

Table 1. Z_{eff} dependence of P_{thr}/P_{thr0} ($\propto Z_{eff}^{\alpha}$) for the data inside n_e window and for all data. Statistical results, mean and σ of P_{thr}/P_{thr0Z} (see equation (3)) and those of P_{thr}/P_{thr0}, are listed.

	ASDEX	AUG	CMOD	DIII-D	JET	JT-60U	Total
number	7	38	40	81	76	62	304
n_{20} window	—	0.31 / 0.43	1.65 / 2.3	0.29 / 0.41	0.23 / 0.40	0.19 / 0.26	—
α_1 (window)	—	0.66	0.79	0.69	0.69	0.80	—
α_2 (all)	1.51	0.72	0.73	0.66	0.69	0.60	0.50
mean (P_{thr}/P_{thr0Z})	1.78	0.86	1.16	1.37	1.18	1.05	1.17
σ (P_{thr}/P_{thr0Z})	0.36	0.20	0.30	0.28	0.41	0.13	0.34
mean (P_{thr}/P_{thr0})	1.76	0.94	1.34	1.00	1.06	1.14	1.10
σ (P_{thr}/P_{thr0})	0.49	0.24	0.68	0.30	0.44	0.22	0.42

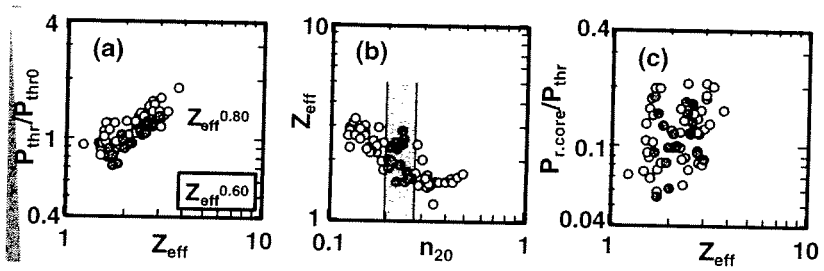

Figure 3. (a) Z_{eff} dependence of P_{thr}/P_{thr0}, (b) relation between n_{20} and Z_{eff}, and (c) relation between Z_{eff} and $P_{r\text{-}core}/P_{thr}$ in JT-60U. Dark circles are data inside a density window. Clear dependence $Z_{eff}^{0.8}$ is seen for these data, and similarly $Z_{eff}^{0.6}$ dependence for all data.

compared with JT-60U data. Values of exponent to Z_{eff} (α) for the data inside n_e window (α_1) and for all data (α_2) are listed in Table 1. They are all near by $\alpha = 0.7$. Now we introduce a scaling basis including Z_{eff} dependence;

$$P_{thr0Z} = P_{thr0} \times (Z_{eff}/2)^{0.7} \qquad (3)$$

Statistical results by the use of this basis are listed in Table 1. We assure that the addition of Z_{eff} dependence into the scaling expression works well to reduce the σ value of (P_{thr}/P_{thrZ}) compared with that of (P_{thr}/P_{thr0}) and to describe principally the rapid increase of P_{thr} in the low-density regime called "low-density anomaly". We find that the change in exponents to B_t, n_{20}, and S is not especially necessary.

We examine the effect of Z_{eff} on the radiation power, and do not especially find the relation between Z_{eff} and $P_{r\text{-}core}$ (radiation power from the core plasma) as shown in figure 3(c). As a result, almost the same dependence, $(P_{thr} - P_{r\text{-}core})/P_{thr0} \sim Z_{eff}^{0.7}$, is obtained. The store of $P_{r\text{-}core}$ in the database is rather poor at present. The analysis considering the effect of $P_{r\text{-}core}$ is the future work. It is interesting to note that equation (3) is similar to a theoretical formula given by Minardi [9], $P_{thr} \sim B_t^{0.97} n_e^{0.77} S Z_{eff}^{0.57}$. Detailed comparison is also the future work.

5. Role of A

As described in section 5, P_{thr} in NSTX is rather large compared with that in standard tokamaks. The $Z_{eff} \sim 2$ in NSTX is not the cause of increased P_{thr}. Nonlinear dependence of P_{thr}

on the aspect ratio A can be true even though the present number of data from low-A tokamaks is not large enough to confirm it. We make bold to propose a example of L-H transition model here. We assume a driving force of the transition is originated by the toroidal effect proportional to the inverse aspect ratio A^{-1}. The parallel flow or current of the untrapped particles plays a key role in the transition mechanism. Therefore we assume also the driving force being proportional to the fraction of untrapped particles $f(A) \approx 1 - \{2/(1+A)\}^{0.5}$. Transition happens more easily for smaller value of $F(A) \propto A/f(A)$. The threshold power to ensure the critical driving force is then supposed to be $P_{thr} \sim F(A)^{\gamma}$. This correction factor takes its minimum at $A \approx 2.7$, and increases rapidly when A approaches unity. This model describes well the results of database analysis. The ratio of P_{thr} to $F(A)^{\gamma} \times P_{thr0*}$ for low-A tokamaks now approaches unity (~1.0 for MAST and ~2.0 for NSTX), where $F(A) = 0.1A/f(A)$ and $\gamma = 0.5 \sim 1$. Verification of the model is the future work together with increasing the amount of low-A data.

6. New scaling and prediction for ITER

Following the above analysis, we present a new scaling expression for P_{thr}.

$$P_{thr,new} = 0.072\, |B|_{out}^{0.7} n_{20}^{0.7} S^{0.9} \times (Z_{eff}/2)^{0.7} F(A)^{\gamma} \qquad (4)$$

where the nonlinear A-dependence term is rather uncertain; $\gamma = 0.5 \pm 0.5$. Figure 4 shows that the new scaling expression (4) fits experimental data better than the P_{thr0} scaling. In figure 4(b), we impose $Z_{eff} = 2$ to COMPASS-D, JFT-2M, MAST, PBX-M, and TCV data. Scattering in the data points is reduced ($\sigma = 0.35$ for $\ln(P_{thr}/P_{thr0})$ and $\sigma = 0.31$ for $\ln(P_{thr}/P_{thr,new})$), and the low-A data points approach the scaling line for the new scaling.

On the basis of the above results, we predict the power threshold in ITER for the standard operation; $R = 6.2$ m, $a = 2$ m, $B_t = 5.3$ T, $I_p = 15$ MA and $S = 680$ m^2 [1]. It is planned to operate the L-H transition at $n_{20} \approx 0.5 \times 10^{20}$m^{-3}. Equation (1) gives $P_{thr0} = 42$ MW, and equation (2) gives $P_{thr0*} = 43$ MW where $|B|_{out} = 4.3$ T is affected only a little by the I_p value. The correction factor $F(A) = 1.03$ in equation (4) changes little the prediction. If Z_{eff} will be kept ~2, $P_{thr} = 40 \sim 50$ MW can be reliable. Effort to decrease impurity will be the key to

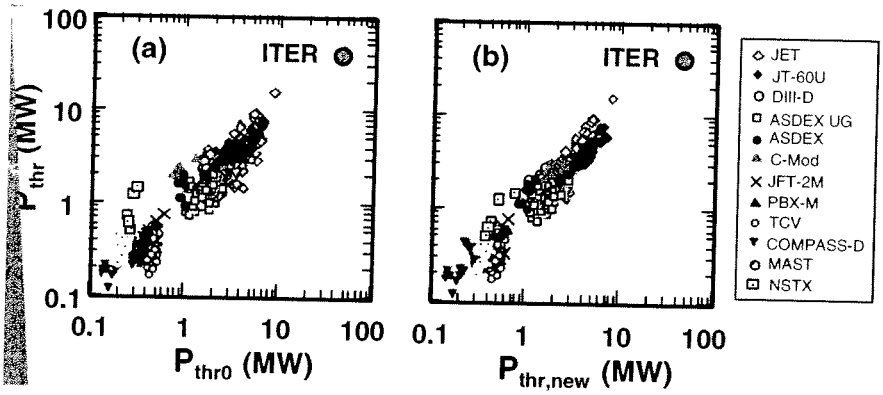

Figure 4. Comparison of experimental P_{thr} data with scaling expression (a) P_{thr0} and (b) $P_{thr,new}$.